Supplementary information

Light-activated interlayer contraction in two-dimensional perovskites for high-efficiency solar cells

Supplementary Discussion

1. Density Functional Theory Our DFT calculations compared the structure of the 2D perovskite crystals (DJ *n*=3, ACI *n*=2, ACI *n*= 3, and RP *n*=3) before and after the injection of a charge (electron or hole) into the lattice (Fig. 2b and Supplementary Fig. 6c). Our results show that upon electron injection, the structures of the three types of 2D perovskite (RP, ACI, DJ) exhibit out-of-plane contraction and in-plane expansion with strain of the same order in both direction, which is incompatible with our experimental results. On the other hand, the ACI perovskites' simulated structures after the injection of one or two holes exhibit anisotropic contraction of their lattice parameters with little change of the Pb-I-Pb angles (Fig. 2b and Supplementary Fig. 6d) which is in good agreement with the experiments. In DJ n=3, our modeling results agree qualitatively with the experiment for one-hole injection only by predicting mainly contraction of the structure in the out-of-plane direction without octahedra tilting and reduction of the organic interlayer spacing. For the RP perovskite, the theory predicts non-negligible strain (>0.1 %) for both electron and hole injection, therefore suggesting that charge accumulation is negligible in the bulk in the RP *n*=3. Conversely, our theory confirms that the DJ and ACI perovskite structures exhibit larger lattice contraction along the stacking direction as compared to in-plane upon hole injection, which we explain by the lower out-of-plane Young's modulus. It also predicts that at equivalent injected charges the light-induced effects are more important in DJ as compared to ACI perovskites, as observed experimentally.

2. X-ray photo-electron spectroscopy analysis. As shown in Fig 2.c and d, Supplementary Fig. 6 a,b, we measured the XPS spectra of the Pb $4f_{7/2}$ and I $3d_{5/2}$ binding states. To exclude any degradation effect, we extract the iodide and lead element ratios before and after light illumination. For DJ =3 mm-sized crystal iodide and lead ratios were 58.27:20.75 versus 58.77:20.23, before and after, respectively. For DJ *n*=3 film iodide and lead ratios were 58.27:20.75 versus 58.77:20.23, before and after, respectively. For RP =3 thin film iodide and lead ratios were 52.14:20.22 versus 52.47:20.47, before and after, respectively. For MAPI 3D thin film iodide and lead ratios were 70.83:29.17 versus 69.77:30.22, before and after, respectively. We observed no shift in the carbon binding energy in all the spectras, nor did we observe the previously reported degradation effects such as traces of metallic lead (Pb^0) states in the DJ and MAPI₃ samples.

3. Space Charge Limited Photocurrent analysis. As shown in Fig. 3b, the space charge limited current was conducted by measuring the J-V trace of the electron only device. We scanned from 0V to 5.5V. In the linear/ohmic region, the conductivity was determined by Ohms law

$$J = \sigma E = \frac{en\mu V}{L}$$

where μ is the mobility, E is the electric field, L is the length of active layer, and σ is the conductivity.[24] We then determine that the sublinear region of the J-V curve was the space-charge limited photocurrent regime due to the fulfillment three criteria proposed by V.D Mihailetchi et.

al, large photogenerated charge carrier generation rate G, long carrier lifetime after dissociation of exciton, the strongly unbalanced of charge transport.[25] The current in this region is given by the following equation

$$J_{ph} = q \left(\frac{9\varepsilon_0 \varepsilon_r \mu}{8q} \right)^{\frac{1}{4}} G^{\frac{3}{4}} V^{\frac{1}{2}}$$

Where ε_0 is the permittivity of free space, ε_r is the dielectric constant, which is 6 for DJ perovskite [26], and q is the electron charge. The trap-filled region was identified by a 3rd order polynomial fit similar to recent reports in perovskites.[24]

4. Percolation model for photo-hole trapping. To support our hypothesis of a percolation-based mechanism, we developed percolation-model of descripting the changes in the mobility. We fit the experimental percolation behavior of the electron mobility, μ_e, as a function of time with a Boltzmann sigmoid empirical law[38-40]:

$$\mu_e(t) = A_{before} + \frac{A_{after} - A_{before}}{1 + e^{(t_0 - t)/b}} \qquad (1)$$

where A_x (x represents "before" or "after") is the mobility before or after light illumination, t_0 is the midpoint time of the sigmoid curve defined as a threshold time, and b is a parameter which allows fitting the steepness of the mobility increase around the threshold. By fitting each of the mobility curves with the same sigmoid function, we extracted the threshold time t_0 and find that t_0 is inversely proportional to the light intensity (Fig. 3g). We describe the onset of the percolation by balancing the rate of generation process with a depopulation process, which is summarized by the following equations:

$$C_t = t_0 G_{eff} \qquad (2)$$
$$G_{eff} = (\alpha G - G_D) \qquad (3)$$

Where G_{eff} is the effective trapping rate of the photogenerated holes, G is the light-induced generation rate per unit volume of photocarriers, which is proportional to the light flux (cm^{-3}/s), α is the photo-hole capture coefficient (cm[3]), and G_D is the depopulation rate of the trapped carriers (1/s). Based on the experimental results in Fig. 4e, we assume that the percolation threshold time t_0 is simply inversely proportional to effective generation rate, through a constant C_t. This constant represents the total number of filled iodide trap sites (unitless) needed to reach the percolation threshold.

$$C_t = t_0 G_{eff} \qquad (2)$$

2

From the fit, we extracted a threshold C_t to be 1.86×10^7 (number of iodide sites), a capture coefficient α to be 2.84×10^{-16} cm^{-3}, and a depopulation density to be G_D 1.96×10^5 s^{-1}. We note that the introduction of a depopulation (carrier detrapping) rate is necessary to reproduce the experimental recovery of the initial mobility once the illumination is switched off (vide infra). Furthermore, in classical semiconductor physics, the physical analogue of α is the carrier capture rate in a recombination and generation (R-G) process for semiconductors and is related capture cross section (σ_p) of a recombination site (defect).[41] In our photogenerated hole trapping system, the iodide sites are the recombination centers and σ_p is the area of an iodide atom (is on the order of 10^{-16} cm^2). Additionally, we note that the depopulation rate G_D is lower than the generation rate times capture coefficient (αG) since we observed a sigmoidal increase for all the light fluxes.

From the two equations above, we rewrite the mobility as a function of generation and depopulation rate:

$$\mu_e(t) = A_{dark} + \frac{A_{light} - A_{dark}}{1 + e^{\left(\frac{C_t}{b(\alpha G - G_D)} - \frac{t}{b}\right)}} \qquad (4)$$

This model is in excellent agreement with our flux dependent SCLC measurements (Fig. 4d). For example, at low fluxes (0.5-Sun and 1-Sun) the midpoint time of growth is large ($t_0 >20$ minutes) due to the fact that the generation rate is on the same order as the depopulation rate ($\alpha G \cong G_D$). At high flux (5-suns) where $G \gg G_D$, the midpoint time of increase is small ($t_0 \cong 1$ minutes). We further verify the percolation model by plotting the dependence of midpoint time of rise against the number of photogenerated carriers (G). Not surprisingly, we find that t_0 is inversely proportional to G (Supplementary Fig. 8c) and can be fitted to a rearranged threshold equation from above.

$$G = \alpha \left(\frac{C_t}{t_0} + G_D\right) \qquad (5)$$

Moreover, we can plot the electron mobility trend as a function of number of trapped holes by using the threshold equation and the fitted values.

$$Number\ of\ carriers\ = t(\alpha G - G_D) \qquad (6)$$

Lastly, the percolation model can also predict the behavior of the mobility relaxation back to its initial value once the illumination is switched off (see Supplementary Fig. 8d for relaxation in dark). The relaxation trend is described by the same law but removing the generation term αG, in the dark. We also note that the typical relaxation time of the sample conductivity is on the same order as the one describing the build-up of the electrical percolation process. They are both characteristic of the collective electrical interconnection of the conductive domains inside the crystal and are not compared to time scales relevant for single hole excitation or relaxation.

Supplementary Table 1 | Summary of the experimental values of both the lattice parameters and unit cell volume measured before and after 51 minutes of continuous light illumination of the samples.

	Out-of-plane parameter			*In-plane parameters*			*Volume*		
	Before (Å)	After (Å)	Strain (%)	Before (Å)	After (Å)	Strain (%)	Before (Å^3)	After (Å^3)	Change (%)
DJ $n=3$	23.12	22.90	0.95	8.85	8.80	0.56	1810.82	1773.38	2.07
ACI $n=3$	43.23	42.98	0.57	6.27	6.24	0.48	3398.99	3347.07	1.55
ACI $n=2$	31.27	31.01	0.83	6.28	6.25	0.46	2466.47	2422.65	1.81
RP $n=3$	50.57	50.57	0.00	8.88	8.88	0.00	3987.67	3987.67	0.00

Supplementary Table 2 | Convention for calculating the net equivalent charges injected in the perovskite systems for the first principle calculations. The 6 octahedra for the DJ compound were used as a reference. $\frac{q_{DJ}}{N_{DJ}} = \frac{q_x}{N_x}$ where $N_{DJ} = 6$ (6 octahedra for DJ), q_{DJ} number of injected charges into the DJ, N_x number of octahedra of the compound for which we would like to obtain the number of injected charges q_x.

	Number of inorganic octahedral	Number of injected charges	Net equivalent charge
DJ n=3	6	1	1
	6	2	2
ACI n=2	16	8/3	1
	16	16/3	2
ACI n=3	24	4	1
	24	8	2
RP n=3	12	2	1
	12	4	2

Supplementary Table 3a | DFT computed structural change in the DJ *n*=3 perovskite for neutral and charged states. Relaxed lattice parameters for the DJ perovskite after charge injection. The percentage error with respect to the reference neutral system is shown between parentheses. The out-of-plane and in-plane directions correspond to the a-axis and bc-plane, respectively.

		Lattice parameters					
	Equivalent net charge	a(Å)	b(Å)	c(Å)	β(º)	Volume (Å^3)	<interlayer I-I> (Å)
Reference neutral	0	22.8729	9.1124	8.2718	90	1724.08	3.88
charged systems	1-	22.8555 (-0.1%)	9.1515 (+0.4%)	8.2781 (+0.1%)	90	1731.45 (+0.4%)	3.86 (-0.5%)
	2-	22.8538 (-0.1%)	9.1979 (+0.9%)	8.2880 (+0.2%)	90	1742.19 (+1.1%)	3.81 (-1.8%)
	--	--	--	--	--	--	--
	1+	22.7765 (-0.4%)	9.1019 (-0.1%)	8.2677 (-0.0%)	90	1713.97 (-0.6%)	3.86 (-0.5%)
	2+	22.3423 (-2.3%)	9.1117 (-0.0%)	8.3281 (+0.7%)	90	1695.61 (-1.7%)	3.62 (-6.7%)

Supplementary Table 3b | DFT computed structural change in the DJ *n*=3 perovskite for neutral and charged states. Relaxed lattice parameters for the DJ perovskite after charge injection. The percentage error with respect to the reference neutral system is shown between parenthesis. The out-of-plane and in-plane directions correspond to the a-axis and bc-plane, respectively.

		Lattice parameters					
	Equivalent net charge	a(Å)	b(Å)	c(Å)	β(°)	Volume (Å³)	<interlayer I-I> (Å)
Reference neutral	0	22.8956	9.0697	8.3146	90	1726.57	3.92
charged systems	1-	22.8523 (-0.2%)	9.1291 (+0.7%)	8.3284 (+0.2%)	90	1737.48 (+0.6%)	3.87 (-1.3%)
	2-	22.8422 (-0.2%)	9.1722 (+1.1%)	8.3339 (+0.2%)	90	1746.07 (+1.1%)	3.83 (-2.3%)
	--	--	--	--	--	--	--
	1+	22.7652 (-0.6%)	9.052 (-0.2%)	8.3077 (-0.1%)	90	1711.96 (-0.8%)	3.89 (-0.8%)
	2+	22.2956 (-2.6%)	9.0829 (+0.1%)	8.3847 (+0.8%)	90	1697.96 (-1.7%)	3.60 (-8.2%)

Supplementary Table 4 | DFT computed structural change in ACI *n*=2 perovskite for neutral and charged states. Relaxed lattice parameters for the ACI perovskite after charge injection. The percentage error with respect to the reference neutral system is shown between parenthesis. The out-of-plane and in-plane directions correspond to the b-axis and ac-plane, respectively.

		Lattice parameters							
	Equivalent net charge	a(Å)	b(Å)	c(Å)	β(°)	Volume (Å³)	<interlayer I-I> (Å)		
							average	min	max
Reference neutral	0	12.6346	30.7063	12.3242	90	4781.29	4.26	3.92	4.47
charged systems	1-	12.7301 (+0.7%)	30.6429 (-0.2%)	12.3356 (+0.1%)	90	4811.94 (+0.6%)	4.25 (-0.2%)	3.91	4.46
	2-	12.8013 (+1.3%)	30.3366 (-1.2%)	12.4521 (+1.0%)	90	4835.74 (+1.1%)	4.19 (-1.6%)	3.88	4.41
	--	--	--	--	--	--	--	--	--
	1+	12.5903 (-0.4%)	30.6180 (-0.3%)	12.3038 (-0.2%)	90	4742.99 (-0.8%)	4.27 (+0.2%)	3.89	4.47
	2+	12.5375 (-0.8%)	30.5143 (-0.6%)	12.3098 (-0.1%)	90	4709.40 (-1.5%)	4.26 (0%)	3.78	4.51

Supplementary Table 5 | DFT computed structural change in ACI *n*=3 perovskite for neutral and charged states. Relaxed lattice parameters for the ACI perovskite after charge injection. The percentage error with respect to the reference neutral system is shown between parenthesis. The out-of-plane and in-plane directions correspond to the c-axis and ab-plane, respectively.

	Equivalent net charge	Lattice parameters				Volume ($Å^3$)	<interlayer I-I> ($Å$)		
		a($Å$)	b($Å$)	c($Å$)	β(º)		average	min	max
Reference neutral	0	12.6686	12.3611	43.0639	90	6743.6887	4.25	4.02	4.47
charged systems	1-	12.7923 (+1.0%)	12.3895 (+0.2%)	42.7700 (-0.7%)	90	6778.62 (+0.5%)	4.22 (-0.7%)	4.02	4.46
	2-	12.8681 (+1.6%)	12.4700 (+0.9%)	42.4982 (-1.3%)	90	6819.46 (+1.1%)	4.19 (-1.4%)	4.01	4.41
	--	--	--	--	--	--	--	--	--
	1+	12.6379 (-0.2%)	12.3212 (-0.3%)	42.9072 (-0.4%)	90	6681.27 (-0.9%)	4.24 (-0.2%)	4.02	4.49
	2+	12.5992 (-0.5%)	12.3017 (-0.5%)	42.7532 (-0.7%)	90	6626.39 (-1.7%)	4.25 (0%)	4.02	4.51

Supplementary Table 6 | DFT computed structural change in RP *n*=3 perovskite for neutral and charged states. Relaxed lattice parameters for the RP perovskite after charge injection. The percentage error with respect to the reference neutral system is shown between parenthesis. The out-of-plane and in-plane directions correspond to the b-axis and abc-plane, respectively.

		Lattice parameters					
	Equivalent net charge	a(Å)	b(Å)	c(Å)	β(°)	Volume (Å^3)	\<interlayer I-I\> (Å)
Reference neutral	0	8.3388	52.4942	9.1261	90	3994.82	> 7
charged systems	1-	8.3561 (+0.2%)	52.5199 (+0.0%)	9.1660 (+0.4%)	90	4022.62 (+0.7%)	> 7
	2-	8.3333(-0.1)	52.1980 (-0.6%)	9.2927 (+1.8%)	90	4042.13 (+1.2%)	> 7
	--	--	--	--	--	--	--
	1+	8.330 (-0.1%)	52.4340 (-0.1%)	9.0784 (-0.5%)	90	3965.56 (-0.7%)	> 7
	2+	8.3255(-0.2%)	52.3146 (-0.3%)	9.0282 (-1.1%)	90	3932.14 (-1.6%)	> 7

Supplementary Table 7 | Comparison of the figures of merit of the DJ and ACI perovskite solar cells between the experimental data (Exp.) and device model (Sim.).

Before	Perovskite	Jsc (mA.cm^{-2})	Voc (V)	FF	PCE (%)
Sim.	DJ n=4	16.18	1.02	0.69	7.99
Expr.	DJ n=4	17.54	1.02	0.72	12.85
Sim.	ACI n=3	14.86	0.92	0.59	7.99
Expr.	ACI n=3	14.79	0.91	0.60	8.04
After	—	—	—	—	—
Sim.	DJ n=4	16.22	1.10	0.76	13.58
Expr.	DJ n=4	17.47	1.10	0.86	16.45
Sim.	ACI n=3	15.00	1.02	0.75	11.55
Expr.	ACI n=3	14.35	1.01	0.76	11.07

Supplementary Table 8 | Equations for Carrier Transport used in the solar cell device model.[10]

Poisson Equation:
$$\epsilon_r \epsilon_0 \nabla^2 \psi = -q\ (n_h - n_e)$$
Continuity:
$$\nabla J_{e,h} = \left(G_{e,h} - R_{e,h}(n_e, n_h) \right)$$
Drift-Diffusion:
$$J_{e,h} = \mu_{e,h} n_{e,h}(-\nabla\psi) \pm D_{e,h}\nabla n_{e,h}$$
Recombination:
$$R_{e,h}(n_e, n_h) = B(n_e n_h - n_i^2) + \frac{n_e n_h - n_i^2}{\tau(n_e + n_h)}$$

Supplementary Table 9 | Absorber parameters for ACI $n=3$ used in the device model.[28-30] "Before" and "after" corresponding to the parameters used before illumination and after 11 minutes under illumination.

Symbol	Description	Parameter value
$L_{Absorber}$	Thickness of absorber layer	200 nm
μ_e	Electron mobility in absorber	**Before:** 10 (cm²/V.s) **After:** 30 (cm²/V.s)
μ_h	Hole mobility in absorber	**Before:** 10 (cm²/V.s) **After:** 30 (cm²/V.s)
τ_e	Electron lifetime in absorber	10 (ns)
τ_h	Hole lifetime in absorber	10 (ns)
$LUMO$	Lowest Unoccupied Molecular Orbital	**Before:** 3.72 (eV) **After:** 3.82 eV
E_G	Band gap of absorber	1.73 (eV)
ε_r	Relative dielectric constant	25
N_A	Self-Doping concentration (P-type)	$1*10^{16}$ (#/cm³)

Supplementary Table 10 | Absorber parameters of DJ *n*=4 used in the device model. "Before" and "after" corresponding to the parameters used before illumination and after 11 minutes under illumination.

Symbol	Description	Parameter value
$L_{Absorber}$	Thickness of absorber layer	200 nm
μ_e	Electron mobility in absorber	**Before:** 10 (cm^2/V.s) **After:** 30 (cm^2/V.s)
μ_h	Hole mobility in absorber	**Before:** 10 (cm^2/V.s) **After:** 30 (cm^2/V.s)
τ_e	Electron lifetime in absorber	10 (ns)
τ_h	Hole lifetime in absorber	10 (ns)
$LUMO$	Lowest Unoccupied Molecular Orbital	**Before:** 3.72 (eV) **After:** 3.81 (eV)
E_G	Band gap of absorber	1.72 (eV)
ε_r	Relative dielectric constant	25
N_A	Self-Doping concentration (P-type)	10^{16} (#/cm^3)

Supplementary Table 11 | Electron transport material parameters (ETM = C60)[31]

Symbol	Description	Parameter value
L_{ETM}	Thickness of ETM layer	30 nm
μ_e	Electron mobility in ETM	10^{-2} (cm^2/V.s)
μ_h	Hole mobility in ETM	10^{-2} $(cm^2/V.s)$

τ_e	Electron lifetime in ETM	1000 (ns)
τ_h	Hole lifetime in ETM	1000 (ns)
$LUMO$	Lowest Unoccupied Molecular Orbital	4.33 (eV)
E_G	Band gap of ETM	2.0 (eV)
ε_r	Relative dielectric constant	4
N_D	Self-Doping concentration (N-type)	$5 * 10^{17}$ (#/cm^3)

Supplementary Table 12 | Hole transport material parameters (HTM = PEDOT:PSS)[32,33]

Symbol	Description	Parameter value
L_{HTM}	Thickness of HTM layer	30 nm
μ_e	Electron mobility in HTM	$9 * 10^{-3}$ (cm^2/V.s)
μ_h	Hole mobility in HTM	$9 * 10^{-3}$ (cm^2/V.s)
τ_e	Electron lifetime in HTM	1000 (ns)
τ_h	Hole lifetime in HTM	1000 (ns)
$HUMO$	Highest Occupied Molecular Orbital	5.18 (eV)
E_G	Band gap of HTM	1.55 (eV)
ε_r	Relative dielectric constant	3
N_A	Self-Doping concentration (P-type)	$3 * 10^{17}$ (#/cm^3)

Supplementary Table 13 | Electron transport material parameters (ETM = PCBM)[35-37]

Symbol	Description	Parameter value
L_{ETM}	Thickness of ETM layer	30 nm

μ_e	Electron mobility in ETM	10^{-2} (cm^2/V.s)
μ_h	Hole mobility in ETM	10^{-2} (cm^2/V.s)
τ_e	Electron lifetime in ETM	1000 (ns)
τ_h	Hole lifetime in ETM	1000 (ns)
$LUMO$	Lowest Unoccupied Molecular Orbital	4.23 (eV)
E_G	Band gap of ETM	2.0 (eV)
ε_r	Relative dielectric constant	4
N_D	Self-Doping concentration (N-type)	$5 * 10^{17}$ (#/cm^3)

Supplementary Table 14 | Bathocuproine layer parameters used in the device model.[31]

Symbol	Description	Parameter value
L_{ETM}	Thickness of ETM layer	1 nm
μ_e	Electron mobility in ETM	10^{-4} (cm^2/V.s)
μ_h	Hole mobility in ETM	10^{-4} (cm^2/V.s)
τ_e	Electron lifetime in ETM	1000 (ns)
τ_h	Hole lifetime in ETM	1000 (ns)
$LUMO$	Lowest Unoccupied Molecular Orbital	4.00 (eV)
E_G	Band gap of ETM	3.5 (eV)
ε_r	Relative dielectric constant	4
N_D	Self-Doping concentration (N-type)	$5 * 10^{17}$ (#/cm^3)

Additional reference

1. Stoumpos C. *et al.* Ruddlesden−Popper Hybrid Lead Iodide Perovskite 2D Homologous Semiconductors. *Chem. Mater.* **28**, 2852−2867. (2016)
2. Soe, C. M. M. *et al.* Structural and thermodynamic limits of layer thickness in 2D halide perovskites. *Proceedings of the National Academy of Sciences*, **116**, 58-66 (2019)
3. Mao. L. *et al.* Hybrid Dion−Jacobson 2D Lead Iodide Perovskites. *J. Am. Chem. Soc. 140*, 3775−3783 (2018)
4. Soe, C. M. M. *et al.* New type of 2D perovskites with Alternating Cations in the Interlayer space, $(C(NH_2)_3)(CH_3NH_3)_nPb_nI_{3n+1}$: Structure, Properties, and Photovolatic Performance. *J. Am. Chem. Soc.* **139**, 16297-16309 (2017)
5. He. X. *et al.* Oriented Growth of Ultrathin Single Crystals of 2D Ruddlesden-Popper Hybrid lead Iodide Perovskite for High-Performance Photodetector. *ACS Appl. Mater. Interfaces.* **11**, 15905−15912 (2019)
6. Sanchez-Bajo, R. and Cumbrera, F.L. The use of the Pseudo-Voigt function in Variance Method of X-ray Line-Broadening Analysis. *J. Applied Crystallography*. **30,** 427-430 (1997)
7. Jiang, Z. *et al*. The dedicated high-resolution grazing-incidence X-ray scattering beamline 8-ID-E at the Advanced Photon Source. *J. Synchrotron Radiat*. **19**, 627–636 (2012)
8. Kevin, Y., *et al.* SciAnalysis. https://github.com/CFN-softbio/SciAnalysis
9. A.L. Patterson, The Scherrer Formula for X-ray Particle Size Determination. *Phys. Rev,* **56**, 10, 978-982, (2019)
10. Smiligies, D-M. Scherrer grain-size analysis adapted to grazing incidence scattering with area detectors. *J. Appl Crystallography*. 42, 1030-1034, (2009)
11. Conings, B. *et al.* Intrinsic Thermal Instability of Methylammonium Lead Trihalide Perovskite. *Adv Energy Mat.* **5**, 1500477-1500485 (2015)
12. Nam, J.K., *et al.* Potassium Incorporation for Enhanced Performance and Stability of Fully Inorganic Cesium Lead Halide Perovskite Solar Cells. *Nano Letters*, **17**, 2028-2033 (2017)
13. Hohenberg, P. and Kohn, W., Inhomogeneous Electron Gas. *Phys. Rev. 136*, B864-B871 (1964)
14. Kohn, W. and Sham, L. J. Self-Consistent Equations Including Exchange and Correlation Effects. **140**, A1133-A1138 (1965)
15. Soler, J. M., *et al.* The SIESTA method for *ab initio* order-*N* materials simulation. *J. Phys. Condens. Matter.* **14**, 2745 (2002)
16. Cooper, V.W. Van der Waals density functional: An appropriate exchange functional. *Phys. Rev. B*. **81**, 161104. (2010)
17. Hamada, I and Otani, M. Comparative van der Waals density functional study of graphene on metal surfaces. *Rev. B*. **82**, 153412. (2010)
18. Yuk, S.F. *et al.* Towards an accurate description of perovskite ferroelectrics: exchange and correlations effects. *Scientific Reports*, **7**, 1738, (2017)

19. Boubacar, T. *et al.* Importance of Vacancies and Doping in Hole-Transporting Nickel Oxide Interface with Halide Perovskites. *ACS Appl. Mater. Interface*, **12**, 5, 6633-6640 (2020)

20. Troullier, N and Martins, J. L. Efficient pseudopotentials for plane-wave calculations. *Phys. Rev. B*, **43**, 1993-2006 (1991)

21. Bitzek, E. *et al.* Structural relaxation made simple. *Phys. Rev. Letter*, **97**, 170201 (2006)

22. Pedesseau, L. *et al.* Advances and Promises of Layered Halied Perovskite Semiconductors. *ACS Nano*, **10**, 11, 9776-9786, (2016)

23. Boubacar, T. *et al.* Composite Nature of Layered Hybrid Perovskites: Assessment on Quantum and Dielectric Confinements and Band Alignment. *ACS Nano*, **12**, 4, 3321-3332 (2018)

24. Mihailetchi, V. D., Wildeman, J. & Blom, P. W. M. Space-Charge Limited Photocurrent. Phys. Rev. Lett. **94**, 126602 (2005).

25. Shi, D. et al. Low trap-state density and long carrier diffusion in organolead trihalide perovskite single crystals. Science 347, 519–522 (2015).

26. Song, B. *et al.* Determination of Dielectric Functions and Exciton Oscillator Strength of Two-Dimensional Hybrid Perovskites. *ACS Mater. Lett.* **3**, 148–159 (2021).

27. Tsai, H. *et al.* Design principles for electronic charge transport in solution-processed vertically stacked 2D perovskite quantum wells. *Nat. Comm.* **9**, 2130 (2018)

28. Stranks, S. D. et al. Electron-Hole Diffusion Lengths Exceeding 1 Micrometer in an Organometal Trihalide Perovskite Absorber. *Science*, **342**, 341 (2013).

29. Brivio, F. *et al.* Structural and electronic properties of hybrid perovskites for high-efficiency thin-film photovoltaics from first-principles. APL Mater. **1**, 042111 (2013).

30. Schulz, P. *et al.* Interface energetics in organo-metal halide perovskite-based photovoltaic cells. *Energy Environ. Sci.* **7**, 1377-1381 (2014).

31. Huang, J. *et al.* Detailed analysis of bathocuproine layer for organic solar cells based on copper phthalocyanine and C60. *Journal of Applied Physics*, vol. 105, no. 7, p. 073105, Apr. 2009, doi: 10.1063/1.3103328.

32. Lenz, A. *et al.* The electronic structure and reflectivity of PEDOT:PSS from density functional theory. *Chem. Phys.* **384**, 44-51 (2011).

33. Rutledge, S. A. and Helmy, A. S. Carrier mobility enhancement in poly(3,4-ethylenedioxythiophene)-poly(styrenesulfonate) having undergone rapid thermal annealing. *J. Appl. Phys.* **114**, 133708 (2013).

34. Trukhanov, V. A. *et al.* Effect of doping on performance of organic solar cells. *Phys. Rev. B* 84, 205318 (2011).

35. Larson, B. W. *et al.* Electron Affinity of Phenyl–C61–Butyric Acid Methyl Ester (PCBM). J. Phys. Chem. C **117**, 14958-14964 (2013)

36. Guan, Z-L. *et al.* Direct determination of the electronic structure of the poly(3-hexylthiophene):phenyl-[6,6]-C61 butyric acid methyl ester blend. *Org. Electron.* **11**, 1779-1785 (2010).

37. Veldman, D. *et al.* Compositional and Electric Field Dependence of the Dissociation of Charge Transfer Excitons in Alternating Polyfluorene Copolymer/Fullerene Blends. *J. Am. Chem. Soc*. **130**, 7721-7735 (2008).

38. Bubnova, O. & Crispin, X. Towards polymer-based organic thermoelectric generators. *Energy Environ. Sci.* **5**, 9345–9362 (2012).

39. Crispin, X. *et al.* The Origin of the High Conductivity of Poly(3,4-ethylenedioxythiophene)−Poly(styrenesulfonate) (PEDOT−PSS) Plastic Electrodes. *Chem. Mater.* **18**, 4354–4360 (2006).

40. .Nevrela, J. *et al.* Secondary doping in poly(3,4-ethylenedioxythiophene):Poly(4-styrenesulfonate) thin films. *J. Polym. Sci. Part B Polym. Phys.* **53**, 1139–1146 (2015)

41. Pierret. R.F. *Advanced Semiconductor Fundamentals,* 150-155, Prentice Hall, (2002).

42. Sidhik, S. *et al.* Memory Seeds Enable High Structural Phase Purity in 2D Perovskite Films for High-Efficiency Devices, *Adv. Mat.*, **33**, 2007176-2007187 (2021).
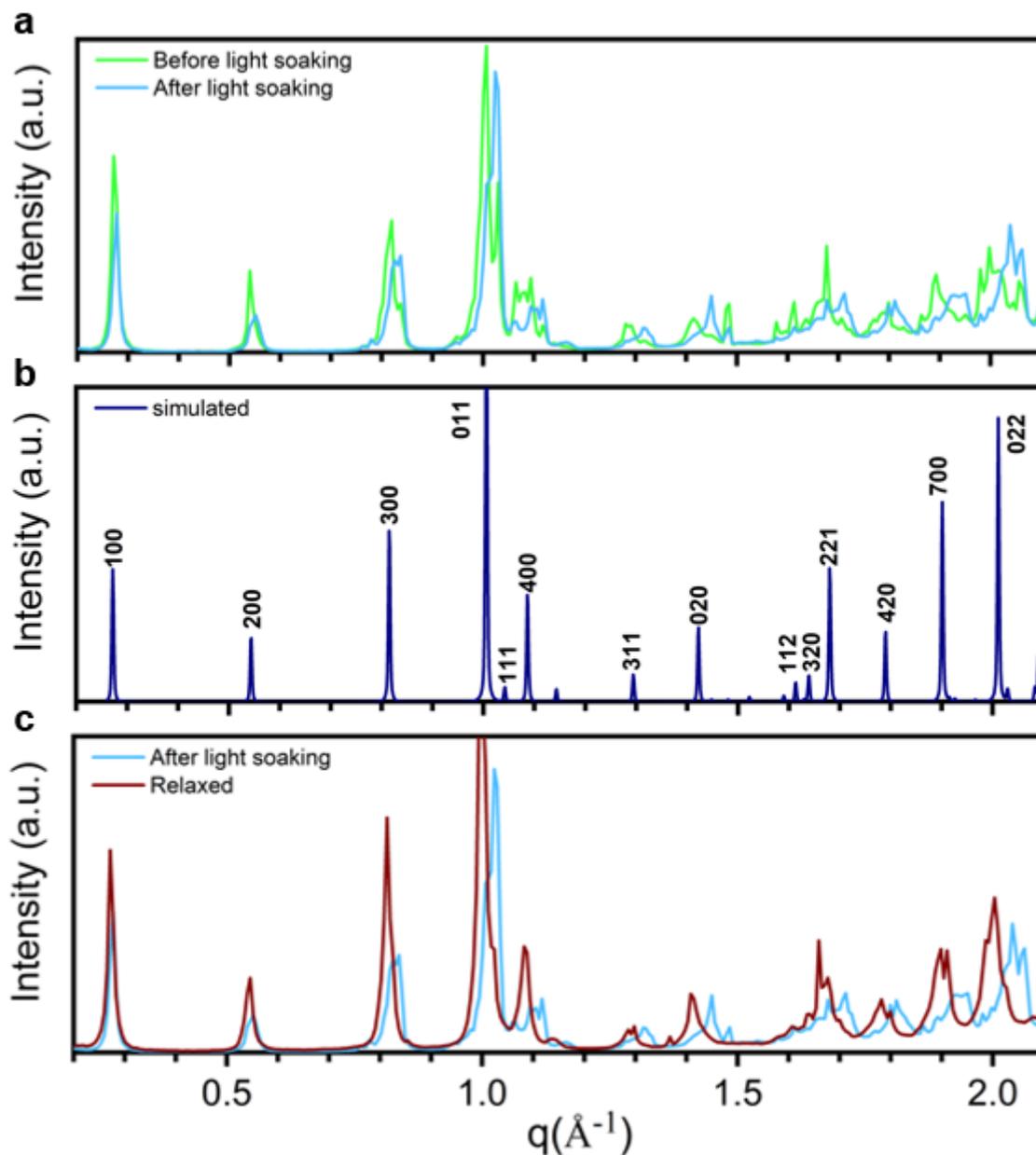
Supplementary Fig. 1 | Structural characterization of Dion-Jacobson (4AMP)MA$_2$Pb$_3$I$_{10}$ perovskite (DJ *n*=3) powders under continuous sunlight illumination. a, Angular-integrated diffraction spectra before and after continuous light illumination for 51 minutes. **b,** Simulated diffraction pattern from the standard crystal structure found in ref. (*3*). The Miller indices hkl are labeled on the graph. **c,** Comparison of the diffraction spectra after 51 minutes illumination and after subsequently resting the samples in the dark for 24 hours.
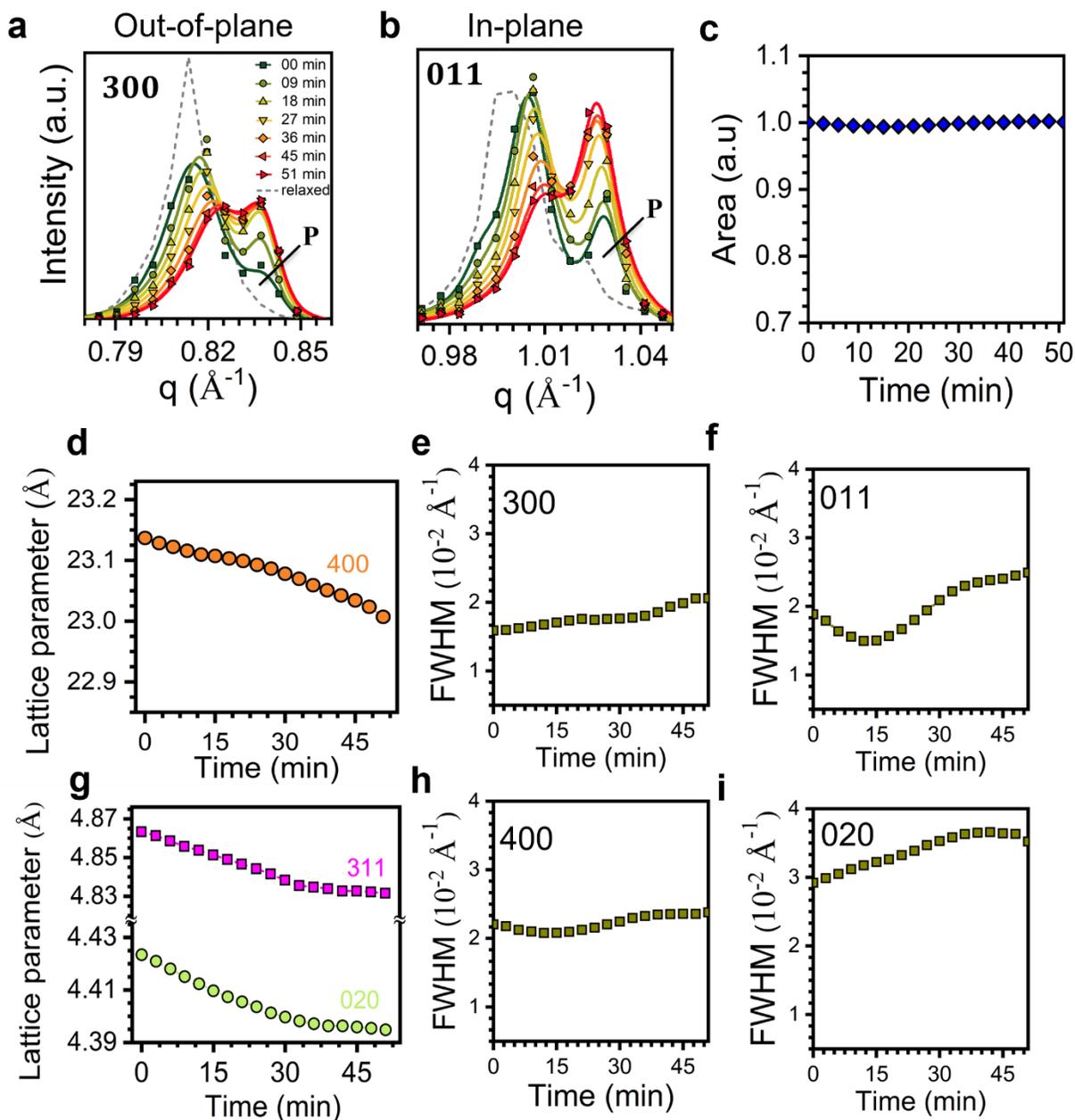
Supplementary Fig. 2 | Extended structural analysis of the DJ *n*=3 under light illumination.
a, Diffraction spectra of the (300) Bragg peak as a function of illumination time. **b,** Diffraction spectra of the (011) Bragg peak as a function of illumination time. The (300) and (011) correspond to the out-of-plane and in-plane directions of the crystals, respectively. "P" indicates the peaks corresponding to a polymorph of DJ *n*=3. The dash line indicates the relaxed spectra. The fits are the solid line and the data is the symbols. **c,** Evolution of the full diffraction intensity of the DJ *n*=3 samples under constant light illumination. **d and g**, Evolution of out-of-plane and in-plane lattice parameters for the (400), (311) and (020) peaks. **e,** Progression of the full-width-at-half-max for the (300) diffraction plane. **f, h, and I,** are the same as **c** for the (011), (400), and (020) planes, respectively.

19
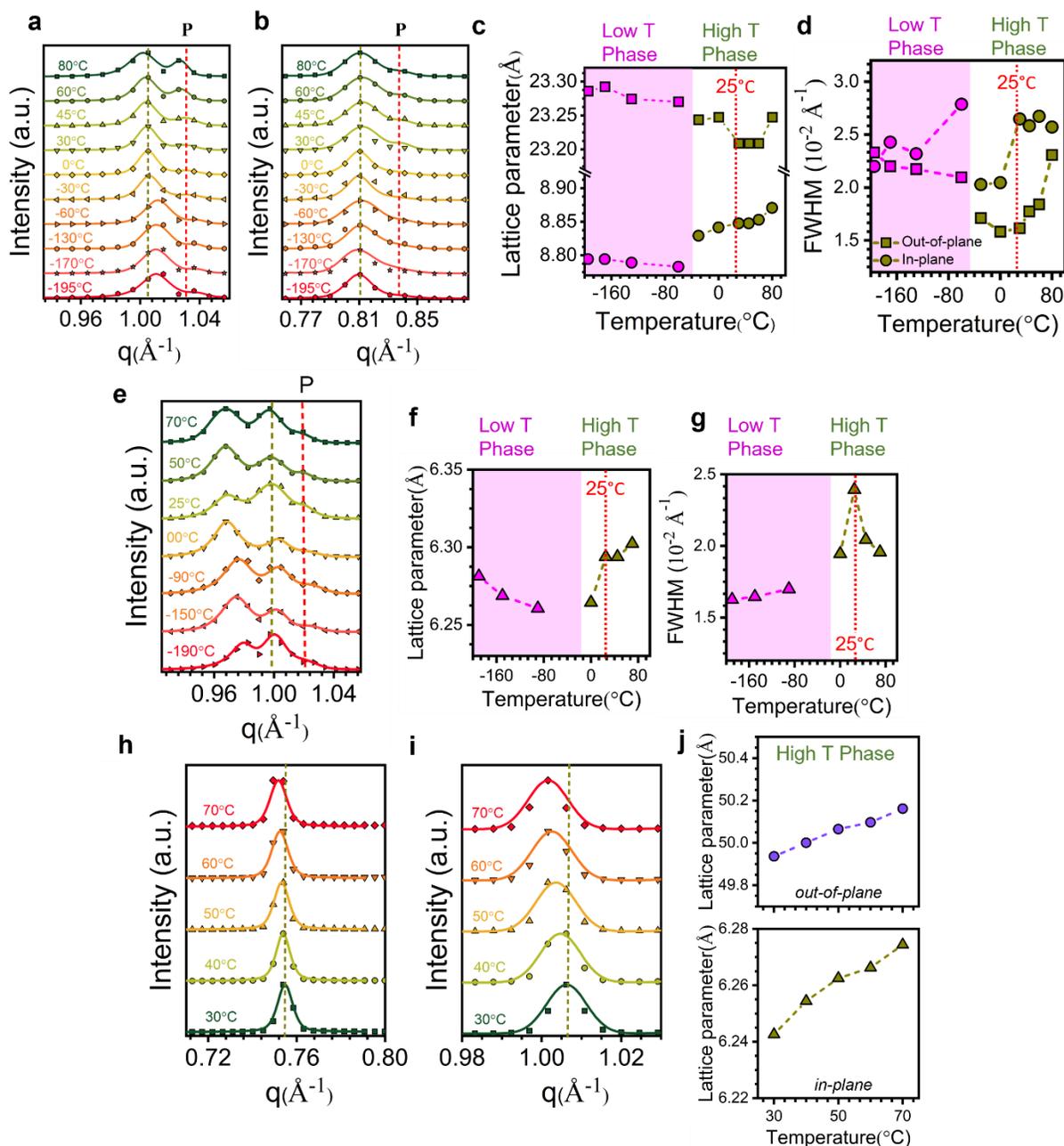
Supplementary Fig. 3 | Temperature dependence of 2D Perovskites. a and b Temperature dependent of DJ *n=3* powder diffraction spectra of the (011) **(a)** and (300) **(b)** planes. **c and d** Corresponding lattice parameter and full-width-at-half-maximum evolution of the out-of-plane and in-plane diffraction peak. The phase transition at about -40°C separate the low temperature phase and high temperature phase of the DJ *n*=3 perovskites. **e,** Temperature dependent of ACI *n=3* powder diffraction spectra of the (101 and 111) plane. **f and g** Corresponding temperature and full-width-at-half-maximum (FWHM) evolution of the out-of-plane (squares) and in-plane (circles) lattice parameters. **h and i,** Temperature dependent of RP *n=3* powder diffraction spectra of the (060) **(h)** and (111) **(i)** plane. **j,** Corresponding lattice parameter for the out-of-plane and in-plane diffraction peak.

20
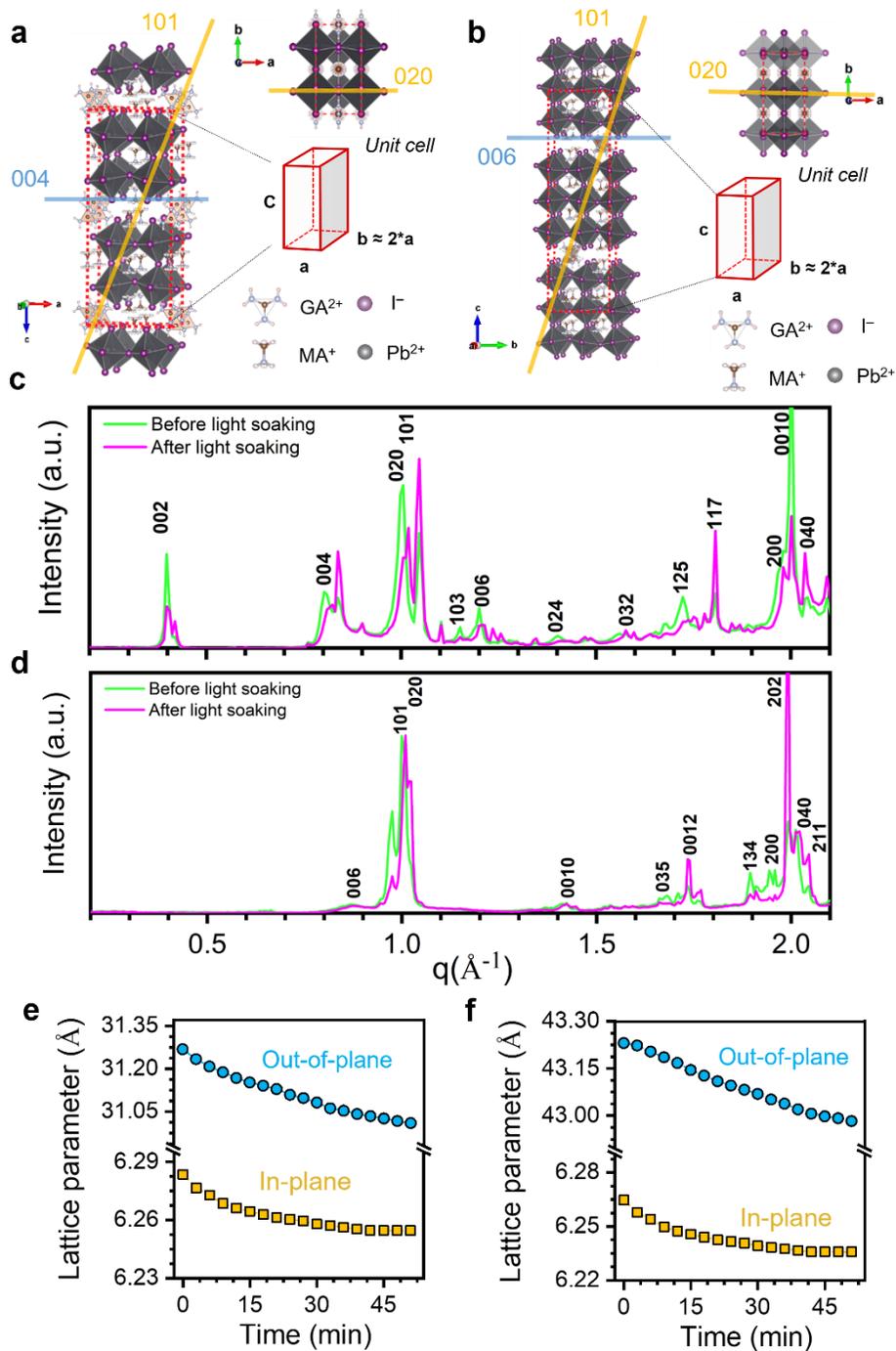
Supplementary Fig. 4 | Evolution of the structure of the Alternating-Cation (GA) MA₂Pb₂I₇ (ACI *n*=2) and Alternating-Cation (GA) MA₃Pb₃I₁₀ (ACI *n*=3) perovskite under light illumination. a and b Structure of the ACI *n* =2 (**a**) and ACI *n*=3 (**b**) perovskites.[4] The unit cell is indicated by the dashed line. **c and d,** Diffraction spectra before and after 51 minutes light illumination for *n*=2 (**c**) and *n*=3 (**d**). **e and f,** Evolution of the lattice parameters as a function of illumination time for *n*=2 (**e**) and *n*=3 (**f**).
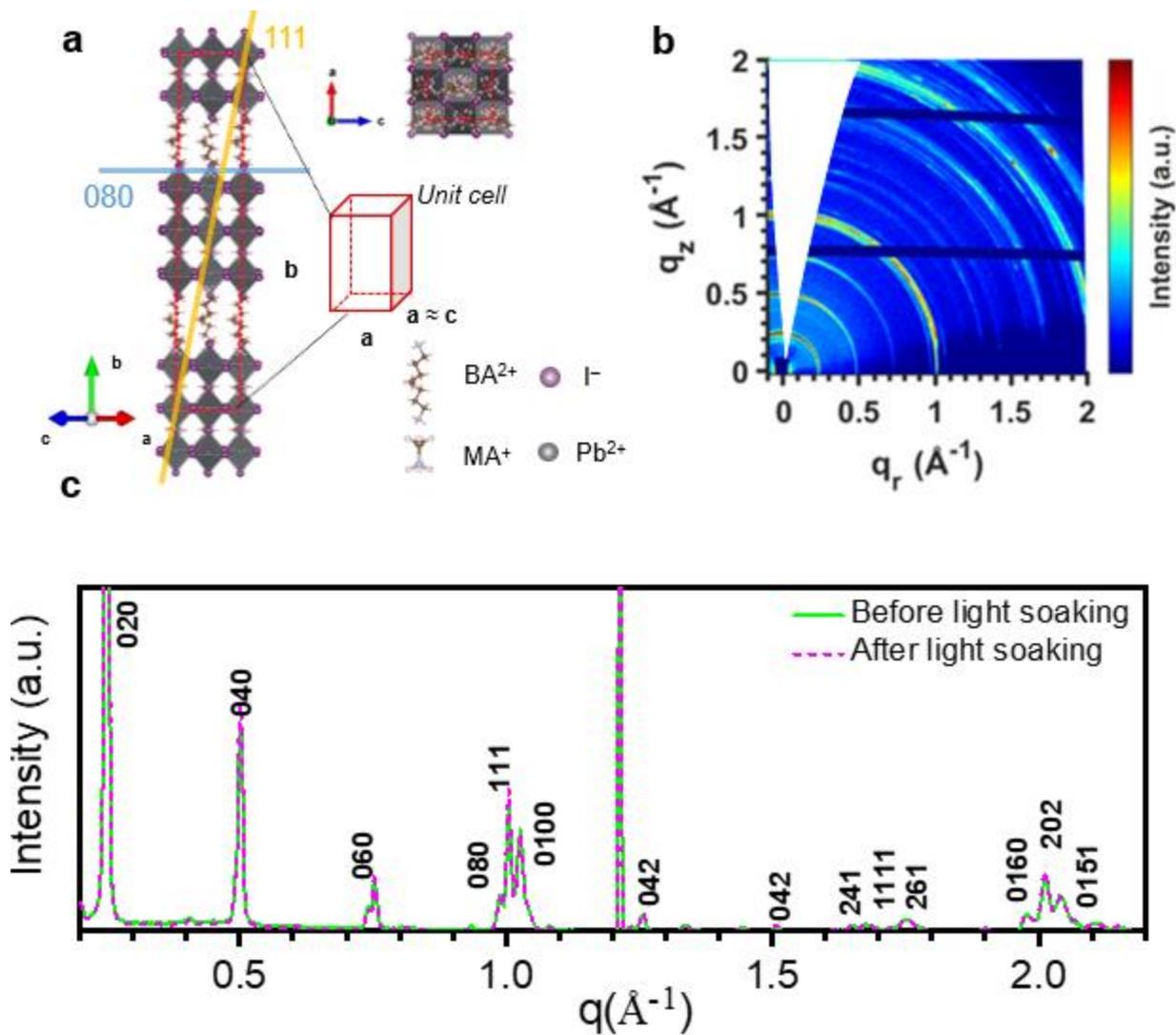
Supplementary Fig. 5 | Evolution of the structure of Ruddlesden-Popper (BA) $_2$ MA$_2$Pb$_3$I$_{10}$ (RP n=3) perovskites under light illumination. a, Structure of the RP n =3 perovskites.[1] The unit cell is indicated by the dashed line. **b,** Example of a typical GIWAXS pattern. **c,** Diffraction spectra before (solid) and after 51 minutes light illumination (dash).
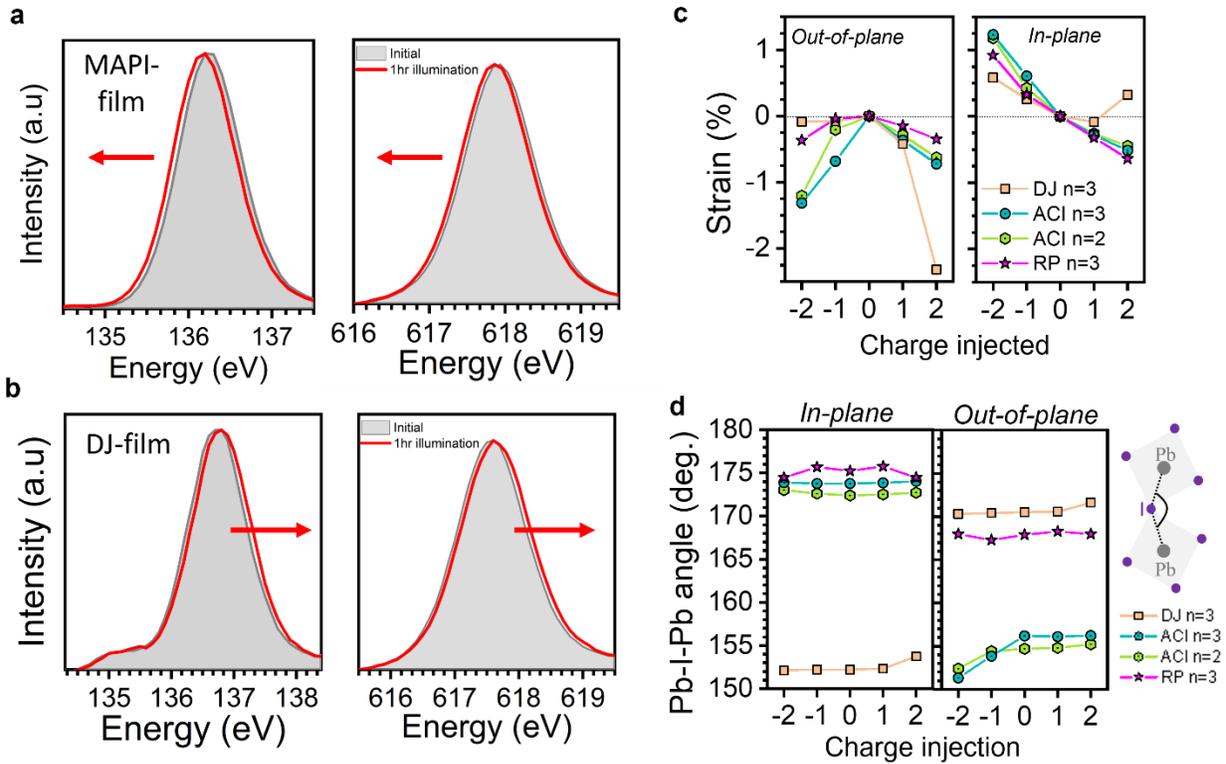
Supplementary Fig. 6 | X-ray photoelectron emission spectroscopy of 3D and 2D perovskite under light and DJ lattice structure as a function of the charge injected in the lattice obtained from first principal calculations. a, Evolution of the Pb^{2+} (left) and I^- (right) photoelectron emission for $MAPbI_3$ perovskite film under light illumination. **b,** Evolution of the Pb^{2+} (left) and I^- (right) photoelectron emission for DJ $n=3$ perovskite film under light illumination. **c,** Calculated strain as a function of the charge injected in the lattice obtained from first principle. **d,** Changes in the in-plane and out-of-plane Pb-I-Pb angle (octahedra tilting) for the DJ, ACI and RP perovskite s as a function of the injected charge. (Right-hand side panel) Schematic of the Pb-I-Pb angle.
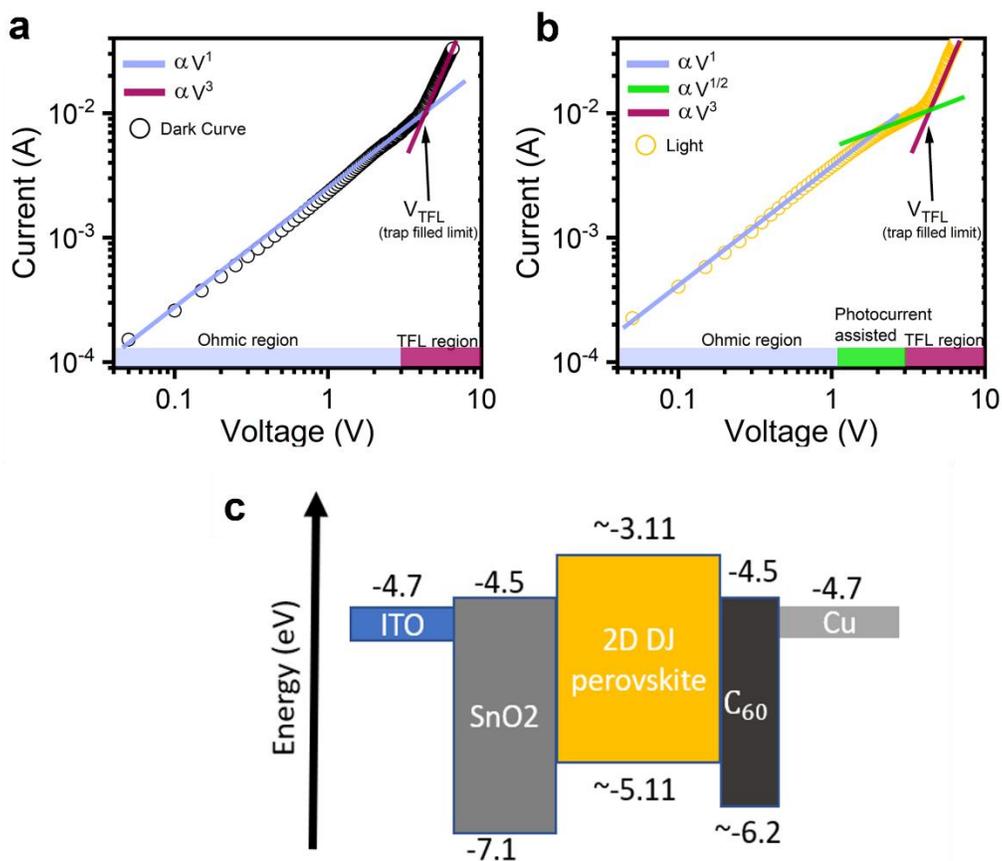
Supplementary Fig. 7 | Dark and illuminated current-voltage traces for electron only device.
a, Current-voltage curve for electron only device in the dark. **b**, Current-voltage curve for electron only device under light. Each panel is marked with the Ohmic, space charge limited photocurrent (photocurrent assisted), and trap filled limit region. **c,** Symmetrical energy band alignment for an electron only device
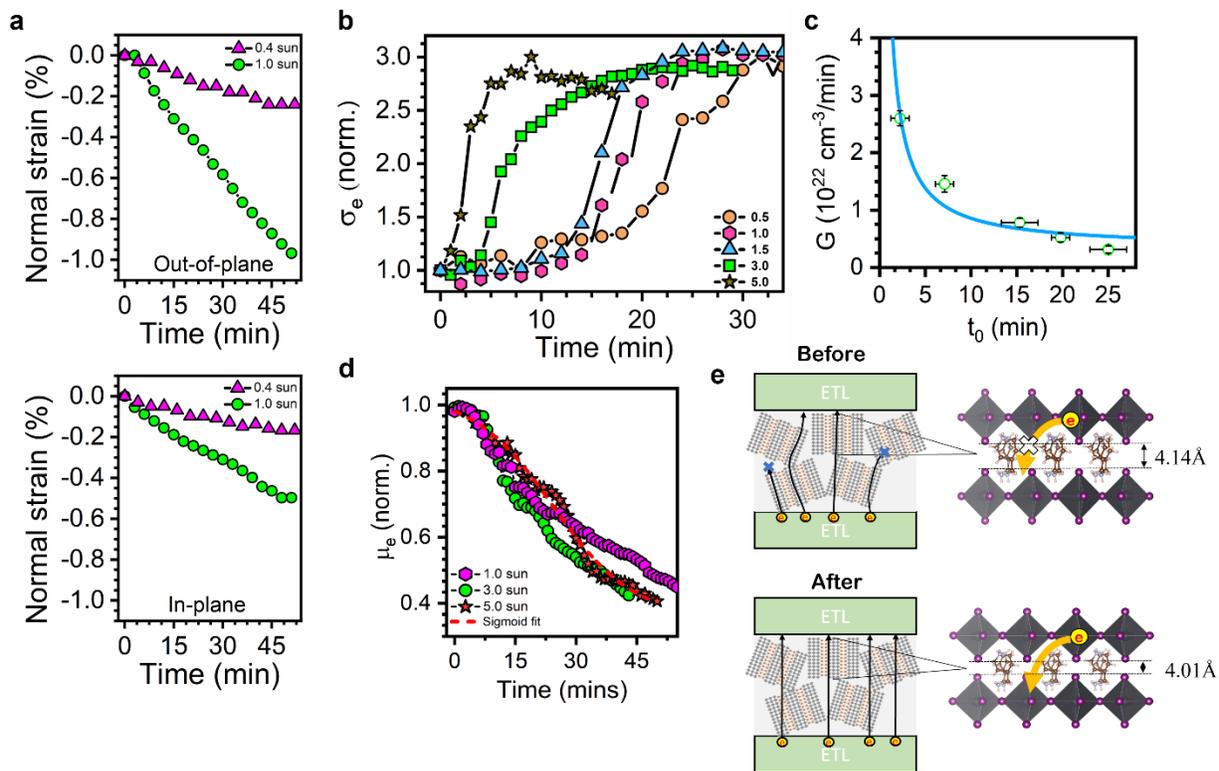
Supplementary Fig. 8 | Intensity dependent GIWAXS and SCLC measurement. a. Evolution of the out-of-plane (top panel) and in-plane (bottom panel) normal strain as a function of light illumination for 0.4 suns and 1.0 suns, respectively. **b,** Flux dependent conductivity as a function of light illumination time. **c,** fitted percolation time threshold as a function of photocarrier generation rate. **d,** Conductivity as a function of relaxation time for different light intensities. **d,** Schematic of the before and after light illumination for the charge transport mechanism.
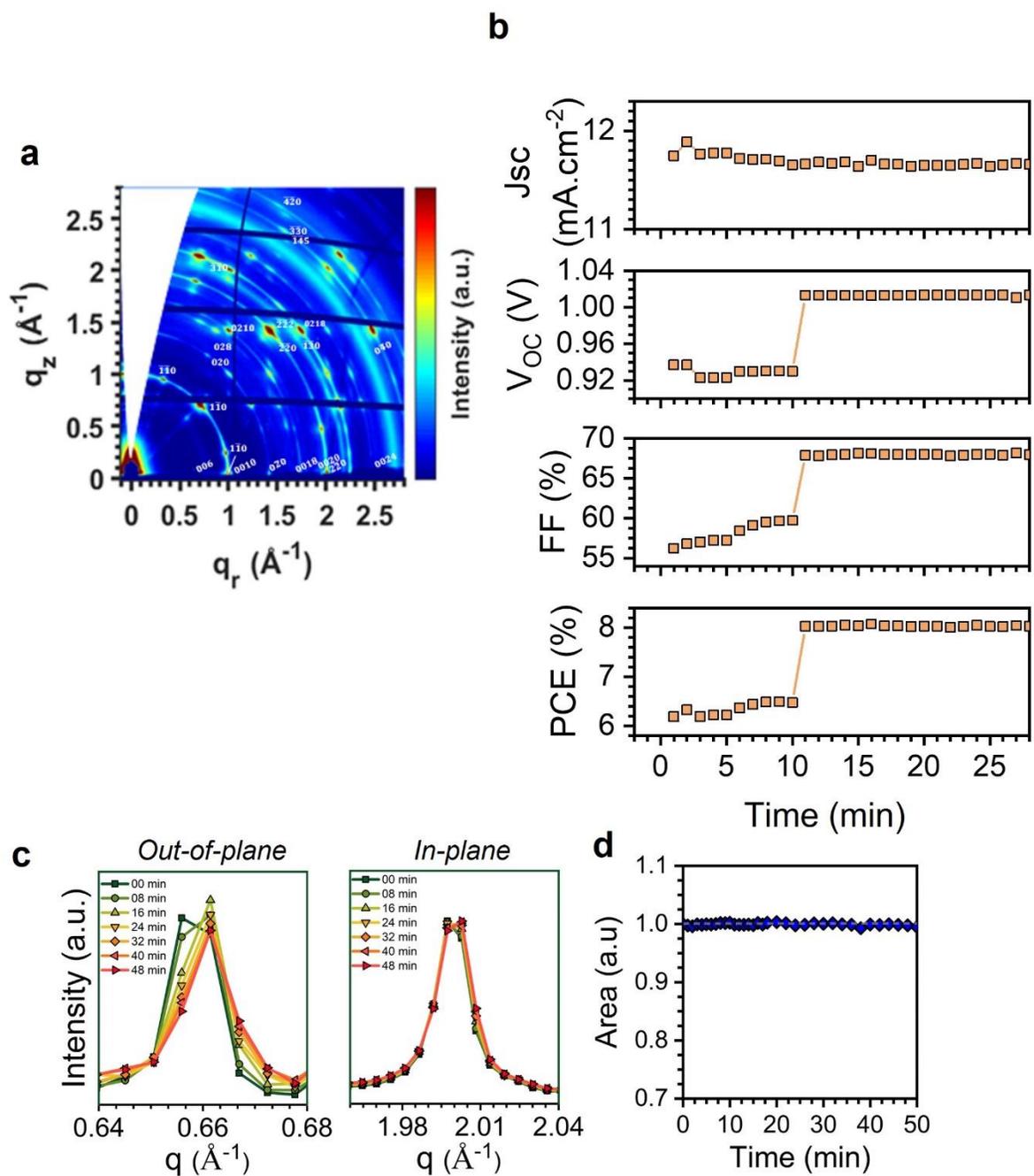
Supplementary Fig. 9 | GIWAXS characterization of DJ thin film and thin-film solar cell device under continuous light illumination. a, Grazing incidence wide-angle x-ray scattering patterns of the thin films solar cell device. Method of indexing can be found in ref [42] **b,** Device performances as a function of illumination time. **c,** Angular-integrated spectra for the out-of-plane and the in-plane as a function of illumination time. **d,** Evolution of total diffraction area under illumination.
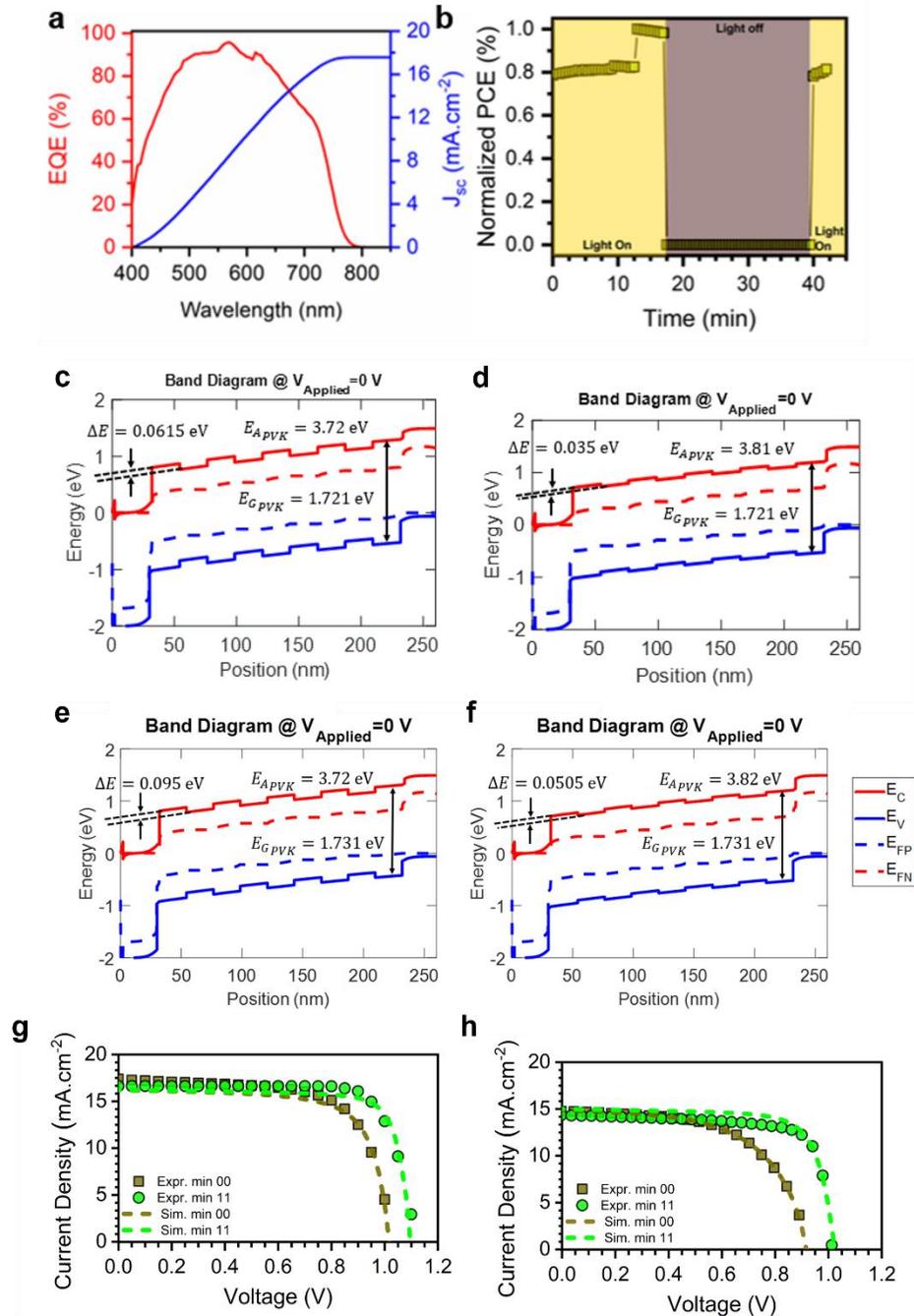
Supplementary Fig. 10 | Device characterization and drift diffusion device modeling. **a,** External quantum efficiency for the DJ *n*=4 perovskite solar cell. **b,** Normalized power conversion efficiency for DJ *n*=4 perovskite device. Cycle plot contains 17 mins of light on and then 23 mins of light off and then 3 mins of light on again. **c,e,** Energy diagram along the perovskite thin films cross-section before light illumination for DJ *n*=4 (**c**) and ACI *n*=3 (**e**). **d,f,** Energy diagram after 11 minutes illumination for DJ *n*=4 (**d**) and ACI *n*=3 (**f**). **g,h,** Comparision of the experimental and simulated current-voltage characteristics at 0 min and after 11 minutes under continuous light illumination for DJ *n*=4 (**g**) and ACI *n*=3 (**h**).